Supplemental Material for: "Unstable slip pulses and earthquake nucleation as a non-equilibrium first-order phase-transition"

Efim A. Brener[1], Michael Aldam[2], Fabian Barras[3], Jean-Frannçois Molinari[3], and Eran Bouchbinder[2]
[1] *Peter Grünberg Institut, Forschungszentrum Jülich, D-52425 Jülich, Germany*
[2] *Chemical and Biological Physics Department, Weizmann Institute of Science, Rehovot 7610001, Israel*
[3] *Civil Engineering Institute, Materials Science and Engineering Institute, Ecole Polytechnique Fédérale de Lausanne, Station 18, CH-1015 Lausanne, Switzerland*

The goal of this document is to provide additional technical details regarding the results reported on in the manuscript.

S-1. The friction law

The friction law used in this work, and whose steady-state behavior is plotted in Fig. 1 in the manuscript, is the same one used previously in [1]. The friction law is defined by the relation between the shear stress $\tau \equiv \sigma_{xy}$ and the compressive normal stress $\sigma \equiv -\sigma_{yy}$ at the interface, $\tau = \sigma \, \mathrm{sgn}(v) f\left(|v|, \phi\right)$, and by the evolution equation for state variable ϕ, $\dot{\phi} = g\left(|v|, \phi\right)$. The constitutive functions $f\left(|v|, \phi\right)$ and $g\left(|v|, \phi\right)$ used in this work take the form

$$f\left(|v|, \phi\right) = \left[1 + b \log\left(1 + \frac{\phi}{\phi_*}\right)\right] \times \left[\frac{f_0}{\sqrt{1 + \left(v_*/v\right)^2}} + \alpha \log\left(1 + \frac{|v|}{v_*}\right)\right] , \tag{S1}$$

$$g\left(|v|, \phi\right) = 1 - \frac{|v| \, \phi}{D} \sqrt{1 + \left(v_*/v\right)^2} , \tag{S2}$$

where ϕ represents the typical age/maturity of contact asperities that compose the spatially-extended interface [2, 3].

Equation (S1) identifies (up to $\log^2$ terms) with the conventional Ruina-Rice rate-and-state friction [4–8], $f \simeq f_0 + f_0 b \log(\phi/\phi_*) + \alpha \log(|v|/v_*)$, if "1" in both log terms in is omitted and $\sqrt{1 + \left(v_*/v\right)^2} \to 1$. Here f_0 sets the scale of the dimensionless frictional resistance (friction coefficient), b is the aging coefficient and α is related to the thermally-activated rheology of contact asperities [2, 3]. In many cases, we have $f_0 b > \alpha$, which implies that steady-state friction (where $\phi = D/|v|$) is velocity-weakening, i.e. f decreases with increasing $|v|$. The constitutive functions $f\left(|v|, \phi\right)$ and $g\left(|v|, \phi\right)$ in Eqs. (S1)-(S2) go beyond the conventional rate-and-state friction relation in three respects; first, the "1" in the α term and the function $1/\sqrt{1 + \left(v_*/v\right)^2}$ that multiplies f_0 (both with a very small v_*) that ensure both that f vanishes as $v \to 0$ and that a low-v velocity-strengthening regime exists prior to the velocity-weakening regime [9]. Second, the "1" in the b term that implies that ϕ_* is a short-time cutoff on logarithmic aging [5, 10, 11], which in turn leads to a high-v minimum in the steady-state f and to another velocity-strengthening regime, as documented for many materials [12]. Third, the function $\sqrt{1 + \left(v_*/v\right)^2}$ that appears also in $g\left(|v|, \phi\right)$, which ensures that for vanishingly small steady-state velocities, ϕ saturates after extremely long times to a finite value of D/v_*, rather than diverges. Note that the authors of [13] invoked a similar regularization of the $\dot{\phi}$ equation; however, while this regularization is crucial for the existence of their 2D steady-state pulse solutions, in our case it makes no difference (even quantitatively the differences are minute) because the steady frictional resistance increases smoothly from zero at vanishing steady-state sliding velocities, hence in the main text we omitted $\sqrt{1 + \left(v_*/v\right)^2}$ from $g\left(|v|, \phi\right)$ (though it is included in the calculations).

S-2. The calculation of the velocity-weakening linear frictional instability nucleation length L_c

The calculation of the nucleation length L_c, associated with the velocity-weakening linear frictional instability, appeared in previous publications (e.g. [1]). The main procedure is repeated here for completeness. We perform a linear stability analysis of an interface steadily sliding at a velocity V. We start with the steady-state frictional relation $\tau = \sigma f_{ss}(V)$, where f_{ss} is plotted in Fig. 1 of the manuscript, from which we obtain

$$\delta\tau = \sigma \delta f + f \delta\sigma = \sigma \left(f_v \delta v + f_\phi \delta\phi\right) + f \delta\sigma , \tag{S3}$$

where we use the shorthand $f_v = \partial_v f$, evaluated at steady-state, and similar notations used for ϕ derivatives and later on for derivatives of g. The normal stress at the interface, σ, is assumed to be constant (i.e. physical mechanisms that generate normal stress variations, such as bi-material contrast [1, 14], are not considered here). In 1D, i.e. in the small height limit, σ at the interface equals, by definition, to $-\sigma_{yy}(y = H)$ [15]. As σ is constant, $\delta\sigma = 0$ and the last term in the above equation can be dropped. We assume that all of the fields are proportional to a Fourier mode $e^{\Lambda t - ikx}$ such that $\delta v = \Lambda \delta u$ and $\delta\phi = \frac{g_v}{\Lambda - g_\phi} \delta v$. Putting it all together, we find

$$\delta\tau = \sigma \left(f_v + f_\phi \frac{g_v}{\Lambda - g_\phi}\right) \Lambda \delta u . \tag{S4}$$

$\delta\tau$ is obtained from the bulk solution [1, 14]. In this work the bulk is described by linear elasticity [16] and for the calculation of L_c we focus on the quasi-static limit, which implies that $\delta\tau$ does not depend on Λ. At the critical wavenumber $k_c = 2\pi/L_c$, we have $\Lambda = i\omega$, and we can decompose Eq. (S4) into its real and imaginary parts

$$G\left(\frac{2\pi}{L_c}\right) + \frac{f_\phi g_v \sigma\omega^2}{g_\phi^2+\omega^2} = 0 \ , \qquad f_v\sigma\omega - \frac{f_\phi g_v g_\phi \sigma\omega}{g_\phi^2+\omega^2} = 0 \ , \tag{S5}$$

where we defined the elastic transfer function $G(k) \equiv \delta\tau/\delta u$. The imaginary part implies

$$\omega^2 = \frac{g_\phi(f_\phi g_v - f_v g_\phi)}{f_v} = -\frac{g_\phi^2}{f_v} f'_{\rm ss}(V) \ , \tag{S6}$$

which means there is a solution only for $f'_{\rm ss}(V) < 0$, i.e. for velocity-weakening friction (note that $f_v > 0$). Substituting this result into the real part above, we obtain

$$G\left(\frac{2\pi}{L_c}\right) = \sigma g_\phi f'_{\rm ss}(V) \ , \tag{S7}$$

from which L_c can be extracted. Note that $g_\phi < 0$.

In the 1D approximation we have $G(k) = \overline{G}Hk^2$ [15], which implies

$$L_c^{(1D)} = 2\pi\sqrt{\frac{\overline{G}H}{\sigma g_\phi f'_{\rm ss}(V)}} \ . \tag{S8}$$

$L_c^{(1D)}$ (without the superscript) is used to normalize quantities of length dimension in the 1D part of the manuscript. In 2D, under mode-III symmetry conditions, we have $G(k) = \mu\,|k|\,/2$, which implies

$$L_c^{(2D)} = \frac{\pi\mu}{\sigma g_\phi f'_{\rm ss}(V)} \ . \tag{S9}$$

$L_c^{(2D)}$ (without the superscript) is used to normalize quantities of length dimension in the 2D part of the manuscript. Finally, note that for $g(|v|,\phi)$ of Eq. (S2), we have $g_\phi = -V/D$ in Eqs. (S8)-(S9) (where $V \gg v_*$ is assumed).

S-3. Scaling theory of $L^*(\tau_{\rm d})$ in 1D and 2D

A simple scaling estimate of the steady-state Eq. (2) in the manuscript reads

$$\frac{\overline{G}\,H}{\beta\,c}\frac{v}{L^*} \sim \tau_{\rm d} - \tau^* \ , \tag{S10}$$

where τ^* is used as the characteristic stress scale and L^* as the characteristic length. A simple scaling estimate of the steady-state Eq. (3) in the manuscript reads

$$\frac{\beta\,c\,\phi}{L^*} \sim \frac{\phi\,v}{D} \ , \tag{S11}$$

where we are interested in the dynamic regime where the aging contribution (the "1" on the RHS) is negligible. Note that ϕ can be eliminated from both sides. Multiplying Eqs. (S10)-(S11), we obtain

$$L^* \sim \sqrt{\frac{\overline{G}\,H\,D}{\tau_{\rm d}-\tau^*}} \ , \tag{S12}$$

which reveals both the scaling of L^* as $\tau_{\rm d} \to \tau^*$ and its dependence on the bulk and interfacial properties.

In the manuscript we use the velocity-weakening nucleation length L_c discussed above to normalize L^*. Using $L_c^{(1D)}$ of Eq. (S8) we obtain

$$\frac{L^*(\tau_{\rm d})}{L_c^{(1D)}} = A_{1D}\sqrt{\frac{\tau^*}{\tau_{\rm d}-\tau^*}} \ , \tag{S13}$$

which is supported by the numerical results in the manuscript, cf. the dashed yellow line in Fig. 3a in which τ^* is explicitly marked and $A_{1D} = 0.314$ is used.

To generate the corresponding scaling estimate in 2D, we need to replace Eq. (2) in the manuscript by its 2D counterpart. The latter is given by the steady-state version of Eq. (S28) below and its scaling estimate reads

$$\frac{v}{\beta\,c_s} \sim \frac{\tau_{\rm d}-\tau^*}{\mu} \ , \tag{S14}$$

where again τ^* is used as the characteristic stress scale. Together with Eq. (S11) (where c is replaced by c_s), which is independent of the spatial dimension, we obtain

$$L^* \sim \frac{\mu\,D}{\tau_{\rm d}-\tau^*} \ . \tag{S15}$$

In fact, this relation can be obtained from the 1D result in Eq. (S12) without any explicit knowledge of the 2D problem. To see this, note that 1D result in Eq. (S12) should cross over to the 2D result for a typical system height H that satisfies $L \sim H$ in both 1D and 2D, directly leading to Eq. (S15). Finally, normalizing by $L_c^{(2D)}$ of Eq. (S9), we obtain

$$\frac{L^*(\tau_{\rm d})}{L_c^{(2D)}} = A_{2D}\frac{\tau^*}{\tau_{\rm d}-\tau^*} \ , \tag{S16}$$

which is in reasonably good agreement with the numerical results in the manuscript, cf. the dashed yellow line in Fig. 5 in which τ^* is explicitly marked and $A_{2D} = 0.430$ is used. Finally, note that the result in Eq. (S16) is in fact valid also in 3D.

S-4. Existence and stability of steady-state travelling solutions in the 1D approximation

In the 1D limit, our equations take the form [15, 17, 18]

$$\partial_t u(x,t) = v(x,t) \ , \tag{S17}$$

$$H\overline{G}\left(c^{-2}\partial_{tt} - \partial_{xx}\right)u(x,t) = \tau_{\rm d} - \sigma f\left[v(x,t),\phi(x,t)\right] \ , \tag{S18}$$

$$\partial_t\phi(x,t) = g\left[v(x,t),\phi(x,t)\right] \ . \tag{S19}$$

A transformation to a co-moving frame of reference, moving at velocity βc, implies $\partial_x \to \partial_\xi$ and $\partial_t \to \partial_t - \beta c \partial_\xi$, where $\xi \equiv x - \beta c t$, leading to the following set of equations

$$(\partial_t - \beta c \partial_\xi)\, u(\xi,t) = v(\xi,t)\ , \tag{S20}$$

$$H\overline{G}\left(c^{-2}\partial_{tt} - 2\beta c^{-1}\partial_{\xi t} - \left(1-\beta^2\right)\partial_{\xi\xi}\right) u(\xi,t) = \tau_{\rm d} - \sigma f\left[v(\xi,t),\phi(\xi,t)\right]\ , \tag{S21}$$

$$(\partial_t - \beta c \partial_\xi)\, \phi(\xi,t) = g\left[v(\xi,t),\phi(\xi,t)\right]\ . \tag{S22}$$

To derive steady-state solutions, we omit all partial time-derivatives from Eqs. (S20)-(S22). Equation (S20) leads to

$$-\beta c \partial_\xi u(\xi) = v(\xi) \quad \Rightarrow \quad u(\xi) = -\frac{1}{\beta c}\int_0^\xi v(\Xi)\, d\Xi\ . \tag{S23}$$

Omitting the time-dependence from Eqs. (S21)-(S22) and substituting the expression for u into Eq. (S21), we end up with two ODE's

$$v'(\xi) = \frac{\beta c}{\left(1-\beta^2\right)H\overline{G}}\left(\tau_{\rm d} - \sigma f\left[v(\xi),\phi(\xi)\right]\right)\ , \tag{S24}$$

$$\phi'(\xi) = -\beta^{-1}c^{-1} g\left[v(\xi),\phi(\xi)\right]\ , \tag{S25}$$

where β, the nonlinear eigenvalue in the problem, is still unknown. This dynamical system can be analyzed using standard tools [19, 20]. That being stated, we do note that Eqs. (S24)-(S25) are generically stiff in the mathematical sense, i.e. they feature widely different scales of variation, and hence even their numerical analysis is nontrivial. This is demonstrated explicitly below.

We first look for the fixed-points of Eqs. (S24)-(S25), i.e. $v'(\xi) = \phi'(\xi) = 0$, which leads to $\{v,\phi\} = \{V, \phi_{\rm ss}(V)\}$ that satisfy $g\left[V,\phi_{\rm ss}(V)\right] = 0$ and $f_{\rm ss}(V) \equiv f\left[V,\phi_{\rm ss}(V)\right] = \tau_{\rm d}/\sigma$. Recall that $f_{SS}(V)$ is shown in Fig. 1 in the manuscript. Since we are looking for solutions which approach prescribed values of V as $\xi \to \pm\infty$, we are interested in the asymptotic behavior of the equations around these fixed-points. A linear stability analysis of Eqs. (S24)-(S25) shows that for $f'_{\rm ss}(V) > 0$, i.e. for V on a velocity-strengthening branch of $f_{\rm ss}(V)$, the fixed-points are in fact saddle points. That is, both eigenvalues are real, one is negative, $\lambda_- < 0$ and one is positive, $\lambda_+ > 0$. The associated eigenvectors are denoted by $\vec{q}_\pm$. This implies that any solution converging to a fixed-point as $\xi \to \pm\infty$ must do so along a particular eigenvector, i.e. $\vec{q}_-$ for $\xi \to +\infty$ ($\lambda_- < 0$ is relevant here in order to avoid divergence in this limit) and $\vec{q}_+$ for $\xi \to -\infty$ ($\lambda_+ > 0$ is relevant here in order to avoid divergence in this limit). With these properties in mind, finding steady-state solutions is straightforward. We integrate Eqs. (S24)-(S25) starting from both large positive and negative values of ξ, using the initial condition $\{v,\phi\} = \{V,\phi_{\rm ss}(V)\} + \varepsilon\vec{q}_\pm$, where ε is a small parameter. We use an initial guess for the value of β, which is improved iteratively using a shooting method [21] (similar to that used in [15, 17]) until the solutions from both ends meet.

An example for the existence of steady-state pulse solutions and their properties, here for $\tau = 1.05\tau_{\rm d}$, is presented in Fig. S1. Here, as we are looking for a slip pulse solution, we demand that both ends of the solution converge to $V_{\rm stick}$. The behavior of the system of equations in the ϕ–v plane, for two close values of β, is considered:

1. **Dashed green line on the left panel**: Here we start integrating from the $V_{\rm stick}$ fixed-point (black circle) along a trajectory that corresponds to a decreasing ξ (starting from a large positive value). The solution first progresses horizontally and then curves down toward the steady-state solution which corresponds to $V_{\rm vw}$ (brown square). For the value of β we use here ($\beta = 0.00333$), the $V_{\rm vw}$ fixed-point is a repeller (for an increasing ξ) and consequently the solution spirals down toward it (because it is a backwards solution, i.e. ξ is decreased).

2. **Solid blue line on the left panel**: Here we start integrating from the $V_{\rm stick}$ fixed-point (black circle) along a trajectory that corresponds to an increasing ξ (starting from a large negative value). This solution curves down toward $V_{\rm vw}$, but avoids it as it is a repeller.

3. **Dashed green line on the right panel**: Here the value of β is slightly increased ($\beta = 0.00334$). We then start integrating from the $V_{\rm stick}$ fixed-point (black circle) along a trajectory that corresponds to a decreasing ξ (starting from a large positive value). The solution initially follows the dashed green line of the left panel, but as it approaches $V_{\rm vw}$, it is repelled away from it.

4. **Solid blue line on the right panel**: The solution initially follows the solid blue line on the left panel, but eventually settles into a finite limit cycle around $V_{\rm vw}$.

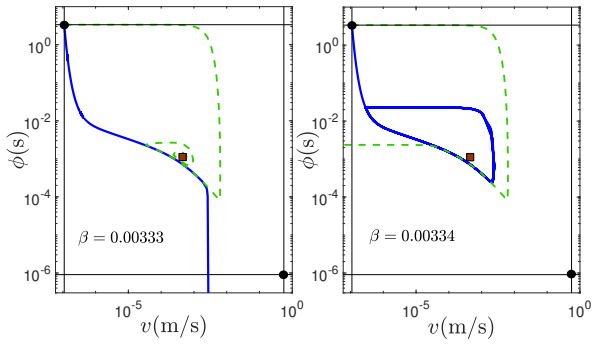

FIG. S1. An example of the existence of a steady-state pulse solution (see details in the text). The left panel is for $\beta = 0.00333$ and the right is for $\beta = 0.00334$.

While the results presented in Fig. S1 do not explicitly demonstrate a steady-state pulse solution, i.e. a trajectory that starts *and* ends at $V_{\rm stick}$, they do demonstrate without doubt that such a solution exists within

an extremely narrow range of β values (here between $\beta = 0.00333$ and $\beta = 0.00334$), which is a manifestation of the stiffness of the underlying equations. To see this, note that phase-plane curves change smoothly as a parameter (in our case β) is varied smoothly. Consequently, there must exist a value of β between $\beta = 0.00333$ and $\beta = 0.00334$ for which the qualitatively different behaviors presented in Fig. S1 are exchanged. At this value of β, which corresponds to a homoclinic bifurcation [19, 20], a homoclinic solution exists, i.e. a solution which starts and ends at the same fixed-point, corresponding to a slip pulse. In fact, the slip pulse solution serves as a separatrix [19, 20] between the two qualitatively different behaviors. The pulse propagation velocity can be estimated as the average between $\beta = 0.00333$ and $\beta = 0.00334$ (note though that the exact pulse propagation velocity does not identify with the value of β for which $V_{\rm vw}$ changes from a repeller to an attractor). The spatial profile of pulse's slip velocity, as shown in Fig. 2 in the manuscript, can be constructed if the trajectories nearly overlap (to an arbitrary accuracy), as in our case. This is demonstrated in Fig. S2. From the spatial profile, we can calculate the width of the pulse, L^*, defined as the distance between the two points where $v(\xi) = V_{\rm vw}$. We also calculate $v_{\rm m}$, which is the maximal velocity of the pulse. The procedure described in this example can be repeated for different τ_d's to obtain the complete spectrum of steady-state slip pulses. A similar procedure is used to derive rupture and healing front solutions.

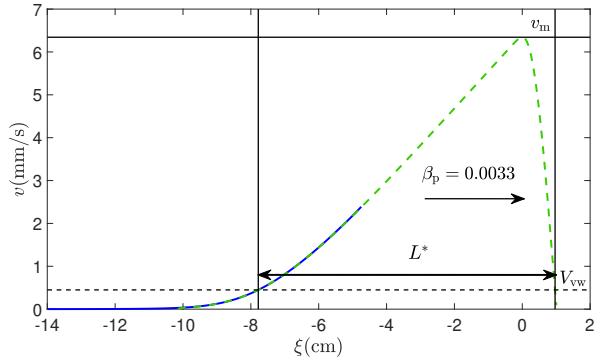

FIG. S2. The same as Fig. 2 in the manuscript (here the dimensional quantities are plotted), except that the two segments corresponding to Fig. S1, are plotted (dashed green and solid blue lines). An almost perfect overlap between the two segments over some spatial range is observed, which justifies plotting a single curve in Fig. 2 in the manuscript.

As described in the manuscript, we next addressed the stability of the steady-state pulse solutions. This is done by solving the partial differential Eqs. (S20)-(S22) through the method of lines [22] and using the perturbation procedure described in the manuscript.

S-5. Steady-state slip pulses as critical nuclei: Perturbations in dynamical calculations

To test the idea that the steady-state slip pulses play the role of non-equilibrium critical nuclei for the onset of rapid slip, we introduced perturbations into the original equations as initial conditions. In 1D, these perturbations are obtained from the steady-state pulse solutions corresponding to $L^*(\tau_{\rm d})$ in the following manner: (i) For $\tau_d > \tau^*$, perturbations with $L > L^*$ are obtained by stretching the steady-state pulse solutions corresponding to a given $\tau_{\rm d}$ and perturbations with $L < L^*$ are obtained by compressing them. (ii) For $\tau_d < \tau^*$, we used the steady-state pulse solutions corresponding to $L = L^*$ as initial conditions, but solved the dynamical equation with values in the range $\tau_d < \tau^*$. We then tracked the system's evolution, by solving Eqs. (S17)-(S19) using the same method of lines [22] mentioned above, for each point in the $L - \tau_{\rm d}$ plane to determine whether the perturbations decay back to $V_{\rm stick}$ or bring the system to $V_{\rm vs}$, resulting in Fig. 3a in the manuscript.

In 2D, we introduced Gaussian perturbations into a steady sliding state at $V_{\rm stick}$. These perturbations are characterized by a width L, corresponding to 10 Gaussian standard deviations (this choice is explained below), and peak amplitude $v_{\rm p}$. The perturbation in ϕ is determined by v through steady-state conditions. The explicit initial conditions take the form

$$v(x,0) = V_{\rm stick} + e^{-\frac{50x^2}{L^2}} \left(v_{\rm p} - V_{\rm stick}\right) \ , \qquad \text{(S26)}$$

$$u(x,0) = 0 \ , \qquad \phi(x,0) = \phi_{\rm ss}(v(x,0)) \ , \qquad \text{(S27)}$$

and are introduced at the center of the domain. We used $v_{\rm p} = 0.167 v_{\rm min}$ (except for the smallest $\tau_{\rm d}$ value for which we used $0.193 v_{\rm min}$). The 2D equations, to be described in more detail in Sect. S-7 below, were solved, leading to Fig. 5 in the manuscript. The robustness of the 2D phase-diagram against variations in the amplitude of the Gaussian perturbations, as long as it is larger than $V_{\rm vw}$, is demonstrated in Fig. S3.

S-6. Steady-state slip pulses for friction curves that feature no minimum

As argued in the manuscript, while it is appealing to think of steady-state slip pulses as emerging from the interaction of steady-state rupture and healing fronts, which vanishes at a finite stress τ^*, this is not a necessary condition. To show this, we consider a steady-state friction curve that features no minimum, for which steady-state rupture and healing fronts — and hence τ^* — do not exist. In particular, we consider f given in Eq. (S1) above, except that we drop the "1" in the ϕ logarithmic term. This change (the $\dot{\phi}$ equation remains unchanged) eliminates the minimum [15, 17], as shown in Fig. S4. We repeated the calculations described above and derived steady-state slip pulse solutions in this case. The results

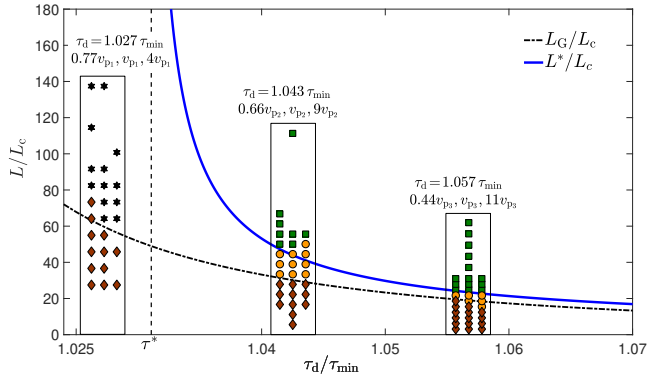

FIG. S3. To demonstrate the robustness of our physical picture against variations in the amplitude of the Gaussian perturbations, we present here results for amplitudes both significantly smaller (yet larger than V_{vw}) and larger than the amplitude used in Fig. 5 in the manuscript. In particular, for three values of τ_d, indicated above each rectangle inside the figure, we used widely different amplitudes (as also indicated above each rectangle, the first one corresponds to the left column, the second one to the middle column and the third one to the right column). The reference amplitude, corresponding to the middle column in each rectangle, is the one used in Fig. 5 in the manuscript (the reference amplitudes are $v_{p_1} = 0.167 v_{min}$ and $v_{p_2} = v_{p_3} = 0.193 v_{min}$). The results (using the same symbol and color codes as in Fig. 5) exhibit negligible variations with the amplitude, further demonstrating the robustness of the 2D phase-diagram using Gaussian perturbations.

for $L^*(\tau_d)$, $v_m(\tau_d)$ and β_p are shown in Fig. S5, together with the results reported in Fig. 3 in the manuscript. We observe that steady-state slip pulses exist in the absence of a minimum in the steady-state friction curve, where the main difference relative to the case in which a minimum exists is the absence of a finite τ^*.

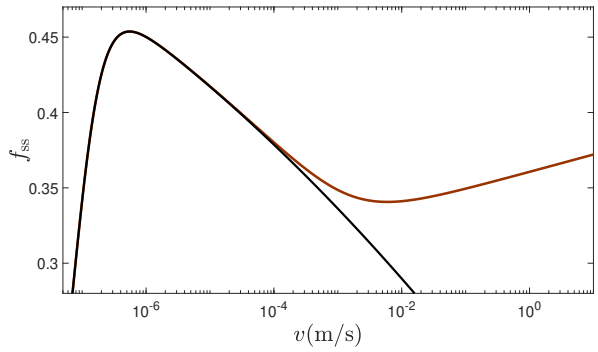

FIG. S4. The steady-state friction coefficient, f_{ss}, corresponding to steady-state conditions in Eq. (S1) (brown line, which is identical to the solid brown line in Fig. 1 in the manuscript). The same, except that the "1" in the ϕ logarithmic term in Eq. (S1) is omitted (black line), resulting in the elimination of the minimum.

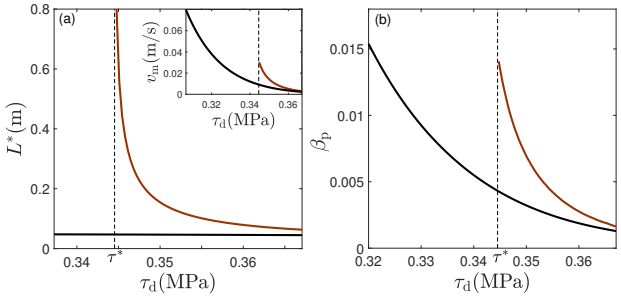

FIG. S5. $L^*(\tau_d)$ (panel a), $v_m(\tau_d)$ (inset panel a) and $\beta_p(\tau_d)$ (panel b) for both the friction curve with a minimum (brown lines here and in Fig. S4) and without (black lines here and in Fig. S4). The brown lines here are identical to the blue lines in Fig. 3 in the manuscript, just without any normalization. The dashed vertical line represents τ^*.

We note in passing that in 2D (and 3D) in infinite systems the radiation of elastic waves from the interface to infinity effectively alters the friction law such that an effective minimum in the steady-state friction relation emerges, even when the bare relation features no minimum. In particular, this radiation process appears as a contribution that is proportional to the slip velocity in the interfacial relation, cf. Eq. (S28) and the text below it. Consequently, we expect such 2D (and 3D) calculations — even in the absence of pure interfacial velocity-strengthening contribution to the bare friction law — to yield qualitatively similar results to ours. Indeed, in [13, 23] such calculations have been performed in the context of searching for self-healing slip pulses; the results indicate the existence of sustained pulses under certain applied stress conditions, which appears to be at least qualitatively consistent with our findings in this context (see Fig. 5 in the manuscript).

S-7. Nucleation in 2D infinite systems under anti-plane shear conditions

As explained in the manuscript, we performed 2D mode-III elastodynamic calculations using the spectral boundary integral formulation [24–26]. The latter relates the traction stresses acting along the interface between two semi-infinite linearly elastic half-spaces and the resulting displacements. For the mode-III elastodynamic problem studied in the manuscript, the interface is initially uniformly pre-stressed by τ_d and set to slide at an extremely small steady velocity V_{stick}, such that the shear tractions at the interface take the form

$$\tau(x,t) = \tau_d - \frac{\mu}{2c_s}\Big(v(x,t) - V_{stick}\Big) + s(x,t)\ . \qquad \text{(S28)}$$

The second right-hand side term represents the instantaneous response to a change in the sliding velocity, the so-called radiation damping term. This term can be understood as the damping of interfacial energy due to elastic waves radiated into the infinite domain. The third

term $s(x,t)$ accounts for the history of interfacial displacements. Both $s(x,t)$ and $u_z(x,t)$ are related in the spectral domain via a convolution integral

$$S(k,t) = -\mu|k| \int_0^t H\Big(|k|c_s(t-t')\Big) U_z(k,t')|k|c_s \, dt' \ , \tag{S29}$$

where $S(k,t)$ and $U_z(k,t)$ are the spatial Fourier transforms of $s(x,t)$ and $u_z(x,t)$, respectively.

In Eq. (S29), the convolution kernel $H(\gamma)$ (not to be confused with the finite system height of previous sections) is expressed from the Bessel function of the first kind $J_1(\gamma)$ as

$$H(\gamma) = \gamma^{-1} J_1(\gamma) \ . \tag{S30}$$

Due to the spectral nature of the formulation, the simulated domain is taken to be periodic, with periodicity X. The latter is chosen to be large enough to prevent any effect of the periodicity on the results reported in the phase-diagram of Fig. 5. The sliding velocity is computed by combining Eq. (S28) and the friction law $\tau = \sigma \, \mathrm{sgn}(v) f(|v|, \phi)$. u_z and ϕ are then integrated in time using an explicit time-stepping scheme

$$u_z(x, t+\Delta t) = u_z(x,t) + 0.5 v(x,t) \Delta t, \tag{S31}$$

$$\phi(x, t+\Delta t) = \phi(x,t) + g\Big(|v(x,t)|, \phi(x,t)\Big)\Delta t \ . \tag{S32}$$

Note that the factor 0.5 on the right-hand-side of Eq. (S31) ensures that $v(x,t)$ is indeed the slip velocity. In order to guarantee the stability and the convergence of the numerical scheme, Δt is defined as the time needed for a shear wave to travel a fraction $\delta = 0.2$ of one grid spacing, i.e. $\Delta t = \delta \Delta x / c_s$.

In Fig. 5 in the manuscript, the Griffith-like length (see manuscript for details)

$$L_{\mathrm{G}} = 4\mu\pi^{-1} G_{\mathrm{c}} \left(\tau_{\mathrm{d}} - \tau_{\mathrm{res}}\right)^{-2} \ , \tag{S33}$$

is plotted (dashed-dotted line). This is made possible once the residual shear stress behind the crack tip during the initial stages of nucleation, τ_{res}, and the effective fracture energy, G_{c}, are calculated. The former, which appears to be nearly constant for a broad range of conditions, is directly extracted from the numerical calculations and takes the value $\tau_{\mathrm{res}} = 0.34$MPa. To calculate G_{c}, we briefly describe a procedure to be discussed in details in [27].

First, note that energy balance near the edge of a front/pulse reads $G_{\mathrm{c}} = G$, where G is the linear elastic energy release rate [28]. G is associated with a near-edge crack-like square root singularity, whose intensity is quantified by the stress intensity factor, K_{III} [28]. In particular, G is related to K_{III} through [28]

$$G = \frac{K_{III}^2}{2\mu\sqrt{1-\beta^2}} \ , \tag{S34}$$

where β, as in the manuscript, is the dimensionless front/pulse propagation velocity (here in units of the shear wave speed $c_s = \sqrt{\mu/\rho}$, where ρ is the mass density). We extract K_{III} from the intermediate asymptotic velocity behind the edge, given by [28]

$$v(r,t) \simeq \frac{2\beta c_s K_{III}(t)}{\mu\sqrt{2\pi\,(1-\beta^2)\,r}} \ , \tag{S35}$$

where r is the distance from the edge. The left panel of Fig. S6 shows three examples of $v(r,t)$, one corresponding to a rupture front (green curves) and two to slip pulses (orange and brown), each features a series of snapshots in time.

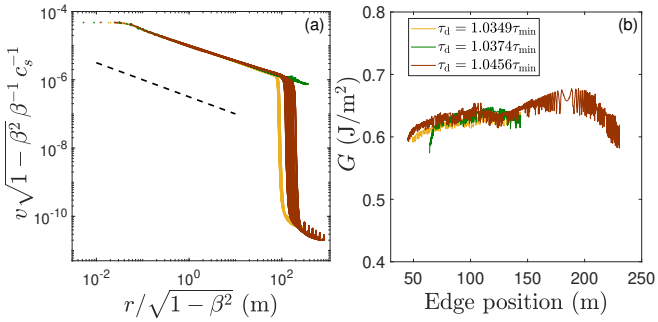

FIG. S6. (a) A normalized $v(r,t)$ vs. a normalized r for a rupture front (green) and two slip pulses (orange and brown) for several times t. The dashed black has a $-1/2$ slope, directly demonstrating the validity of the intermediate asymptotic relation in Eq. (S35). (b) The corresponding energy release G, calculated through Eq. (S34) once K_{III} is extracted from (a), vs. the edge position.

In all examples, there exists a spatial range where $v \propto 1/\sqrt{r}$ (black dashed line, a guide to the eye), as expected. By extracting $K_{III}(t)$ from these curves, we can calculate $G(t)$ through Eq. (S34). The result, where G is plotted as a function of the front/pulse edge position (not time t), is shown on the right panel of Fig. S6. We observe that G varies only slightly during propagation, and hence we approximate it by a constant $G_{\mathrm{c}} = 0.65\mathrm{J/m}^2$, used to calculate L_{G} through Eq. (S33). We note that while an edge singularity does not exist in 1D, global energy balance considerations can still be used to define a Griffith-like length, which in this case scales as $\sqrt{G\,H\,G_c}\,(\tau_{\mathrm{d}} - \tau_{\mathrm{res}})^{-1}$ [29]. We extensively searched for signatures of the 1D Griffith-like length in our 1D analysis, but found none.

The results of our 2D mode-III calculations are summarized in the phase-diagram in Fig. 5 in the manuscript. The Gaussian perturbations procedure is described above in Sect. S-5. Note that the width of perturbations L is defined to correspond to 10 standard deviations so that L_{G} indeed separates decaying from propagating perturbations (see manuscript for details) for a *single* value of τ_{d}. Finally, the phase-diagram features 4 different dynamical behaviors ("phases"), denoted by different symbols and colors in Fig. 5 in the manuscript. We verified that the phase-diagram is independent of the amplitude of perturbations, as long as it is larger than V_{vw},

see Fig. S3. We attach to this Supplemental Material 4 movies, each corresponds to a different dynamical behavior ("phase"), according to the following list:

- **Movie_S1:** Decay without propagation arising for $L < L_G$ (brown diamonds in Fig. 5).
- **Movie_S2:** Nucleation arising for $L > L^*$ (green squares in Fig. 5).
- **Movie_S3:** Decay with propagation arising for $L > L_G$ and $\tau_d < \tau^*$ (black hexagrams in Fig. 5).
- **Movie_S4:** Sustained pulses arising for $L_G < L < L^*$ and $\tau_d > \tau^*$ (orange circles in Fig. 5).

Note that in the movies V_{vw} and V_{vs} correspond to the steady-state solutions of Eq. (S28), i.e. $\sigma f(v, \phi = D/v) = \tau_d - \frac{\mu}{2c_s}(v - V_{stick})$, which do not identify with those defined in Fig. 1 in the manuscript.

Finally, we note that propagation velocities, both of rupture fronts and of pulses, are generally larger in 2D compared to 1D. To see this, note that Eq. (S11) is dimension-independent and takes the form $\beta \sim \frac{Lv}{Dc_s}$, where L is the characteristic size and v is the characteristic slip rate. L is known to increase with the system size H before it saturates to an H-independent value (in the small H regime it scales with $\sqrt{H}$) and hence is larger in 2D than in 1D. In addition, the slip rate v is expected to be larger in 2D in the presence of a crack-like tip singularity (which is absent in 1D). Finally, the presence of velocity-strengthening friction also affects the propagation speed. In particular, in the absence of velocity-strengthening friction, as discussed in Section S-6 above, both the maximal slip rate (inset of Fig. S5a) and the propagation velocity (Fig. S5b, note as τ^* does not exist for pure velocity-weakening friction, decreasing the driving stress τ_d will lead to an increase in the propagation velocity) increase.

S-8. Parameters

The parameters used for all the calculations described in the manuscript and here are given in Table I. Note that the values of the listed parameters are characteristic of some laboratory experiments (see [12] for details). However, the generic properties of the derived results are independent of the exact numbers, and are relevant to a broad range of materials and physical situations. For example, v_* that controls the velocity scale below which the system is in the stick phase, can be taken to be significantly smaller, and larger confining pressures σ can be considered.

Parameter	Value	Units
$\overline{G}, \mu$	9×10^9	Pa
H	2×10^{-4}	m
σ	10^6	Pa
c, c_s	2739	m/s
D	5×10^{-7}	m
b	0.075	-
v_*	10^{-7}	m/s
f_0	0.28	-
ϕ_*	3.3×10^{-4}	s
α	0.005	-

TABLE I. Values for all parameters used (in MKS units).

[1] M. Aldam, M. Weikamp, R. Spatschek, E. A. Brener, and E. Bouchbinder, Geophys. Res. Lett. **44**, 11,390 (2017).
[2] T. Baumberger and C. Caroli, Adv. Phys. **55**, 279 (2006).
[3] T. Putelat, J. H. Dawes, and J. R. Willis, J. Mech. Phys. Solids **59**, 1062 (2011).
[4] A. L. Ruina, J. Geophys. Res. Solid Earth **88**, 10359 (1983).
[5] C. Marone, Nature **391**, 69 (1998).
[6] C. Marone, Annu. Rev. Earth Planet. Sci. **26**, 643 (1998).
[7] M. Nakatani, J. Geophys. Res. Solid Earth **106**, 13347 (2001).
[8] P. Bhattacharya and A. M. Rubin, J. Geophys. Res. Solid Earth **119**, 2272 (2014).
[9] Y. Estrin and Y. Bréchet, Pure Appl. Geophys. **147**, 745 (1996).
[10] M. Nakatani and C. H. Scholz, J. Geophys. Res. Solid Earth **111**, 1 (2006).
[11] O. Ben-David, S. M. Rubinstein, and J. Fineberg, Nature **463**, 76 (2010).
[12] Y. Bar-Sinai, R. Spatschek, E. A. Brener, and E. Bouchbinder, J. Geophys. Res. Solid Earth **119**, 1738 (2014).
[13] G. Perrin, J. R. Rice, and G. Zheng, J. Mech. Phys. Solids **43**, 1461 (1995).
[14] M. Aldam, Y. Bar-Sinai, I. Svetlizky, E. A. Brener, J. Fineberg, and E. Bouchbinder, Phys. Rev. X **6**, 041023 (2016).
[15] Y. Bar-Sinai, R. Spatschek, E. A. Brener, and E. Bouchbinder, Phys. Rev. E **88**, 060403 (2013).
[16] L. D. Landau and E. M. Lifshitz, *Theory of Elasticity*, 3rd ed. (Pergamon Press, London, 1986).
[17] Y. Bar Sinai, E. A. Brener, and E. Bouchbinder, Geophys. Res. Lett. **39**, L03308 (2012).
[18] T. Putelat, J. H. Dawes, and A. R. Champneys, Proc. R. Soc. A Math. Phys. Eng. Sci. **473**, 20160606 (2017).
[19] J. Meiss, *Differential dynamical systems* (Siam, 2007).
[20] S. H. Strogatz, *Nonlinear dynamics and chaos: With applications to physics, biology, chemistry, and engineering*, 2nd ed. (Westview press, 2014).
[21] W. H. Press, S. A. Teukolsky, W. T. Vetterling, and B. P. Flannery, *Numerical recipes 3rd edition: The art of*

scientic computing (Cambridge University Press, 2007).
[22] W. E. Schiesser, *The numerical method of lines: Integration of partial differential equations*, 1st ed. (Academic Press, 1991).
[23] G. Zheng and J. R. Rice, Bull. Seismol. Soc. Am. **88**, 1466 (1998).
[24] P. H. Geubelle and J. R. Rice, J. Mech. Phys. Solids **43**, 1791 (1995).
[25] J. W. Morrissey and P. H. Geubelle, Int. J. Numer. Methods Eng. **40**, 1181 (1997).
[26] M. S. Breitenfeld and P. H. Geubelle, Int. J. Fract. **93**, 13 (1998).
[27] F. Barras, M. Aldam, E. A. Brener, E. Bouchbinder, and J.-F. Molinari, To be published (2018).
[28] L. B. Freund, *Dynamic fracture mechanics* (Cambridge university press, New York, 1998).
[29] A. Puzrin and L. Germanovich, Proc. R. Soc. A Math. Phys. Eng. Sci. **461**, 1199 (2005).